



Densification of nanoporous metals during nanoindentation: The role of structural and mechanical properties

N. Huber^{1,2,a)} , I. Ryl^{1,2}, Y. Wu¹, M. Hablitzel¹, B. Zandersons², C. Richert¹, E. Lilleodden^{1,3}

¹Institute of Materials Mechanics, Helmholtz-Zentrum Hereon, Geesthacht, Germany

²Institute of Materials Physics and Technology, Hamburg University of Technology, Hamburg, Germany

³Institute of Advanced Ceramics, Hamburg University of Technology, Hamburg, Germany

^{a)}Address all correspondence to this author. e-mail: norbert.huber@hereon.de

Received: 29 July 2022; accepted: 12 December 2022; published online: 4 January 2023

The analysis of the densification behavior of nanoporous metals in nanoindentation is challenging in simulations and experiments. A deeper understanding of the densification behavior provides valuable information about the different deformation mechanisms in nanoindentation and compression experiments. The developed two-scale model allows for predicting the densification field for variable microstructure and elastic–plastic behavior. It could be shown that the penetration depth of the densification field is mainly controlled by the ratio of the macroscopic work hardening rate to yield stress. The shape as well as the value at characteristic isolines of densification depend mainly on the macroscopic plastic response of the nanoporous material. This could be confirmed by nanoindentation experiments, where the densification under the indenter was measured for ligament sizes from 35 to 150 nm. Although the depth of the densification field was underpredicted by the simulations, the experiments confirmed the predicted trends.

Introduction

Nanoporous gold (np-Au) is an ideal model material for fundamental research on structure–property relationships of open pore materials. Macroscopic samples can be produced by dealloying, exhibiting a bicontinuous network of nanoscale pores and solid ligaments connected in junctions. An overview of the fascinating morphologies and mechanical properties of this material is provided in review articles [1–3]. The average diameter of the ligaments and their connectivity density can be controlled by altering the dealloying conditions followed by a heat treatment, thereby allowing to examine the impact of the ligament size, load-bearing rings, and effective solid fraction on the macroscopic mechanical properties [4–7].

Due to the nanoscale nature of the materials, a direct access to the elastic–plastic mechanical properties of the solid phase that makes up the ligaments and nodes of the metal network is not possible. Insights can only be gained indirectly via nanoindentation [4, 8, 9], micropillar testing [8, 10] or macroscopic compression [11–15]. In all cases—even for the micromechanical tests—the experiment averages over a considerable number

of features which are of random nature, and the interpretation requires models that are based on abstraction and simplification of the complex network structure. Commonly, the Gibson–Ashby scaling laws [16], modifications of them or numerical simulations are applied. For an overview the reader is referred to [17].

In contrast to micropillar compression and macrocompression testing, the inhomogeneous deformation in nanoindentation requires additional assumptions for the interpretation of the load–displacement data, concerning the plastic compressibility of the material. Biener et al. reported that deformation is confined in the contact area and is dominated by a ductile densification, while the pore structure adjacent to the indents remained undisturbed [4]. The authors assumed that the contact depth h_c is equal to the indentation depth h , as there is no elastic deformation adjacent to the contact for the densifying material, and the material can be idealized as “rigid–perfectly plastic” in compression. It can be argued that the distribution of the densification under the indenter and perhaps also in its vicinity depends on the ligament size and further mechanical or

microstructural parameters. Therefore, an in-depth investigation of the densification behavior under an indenter is of fundamental importance. However, the measurement of the densification after nanoindentation is challenging and only a few works exist in literature.

Leitner et al. measured the densification in np-Au for nanoindentation at room temperature and after loading at high temperature [18]. They computed porosity maps from segmented images of cross-sections prepared with a focused ion beam (FIB). It is found that the densification remains localized close to the tip in the room temperature test, whereas for the high temperature test slightly denser zones are observed that are almost equally distributed over a large region extending beyond the contact radius. Briot and Balk prepared a cross-section of np-Au sample after nanoindentation in np-Au and measured the densification as function of the depth that relates to the distance of parabolic segments to the indenter tip [19]. The results suggest a maximum densification below the surface while full structural densification directly under the indenter was not detected. Moreover, the extent of deformation ahead of the indenter was remarkable and the authors concluded that the behavior of np-Au during nanoindentation behaves more like a dense metal than a low-density porous material, which is in agreement with [11]. Recently, Richert et al. improved the approach for the image processing after FIB cross-sectioning such that the quality of the segmentation is comparable to a tedious manual approach [20]. They were able to derive densification scans starting from the indenter tip along the contact surface and into the depth and concluded that the extracted densification profiles show an overall increasing densification towards the indenter tip that can be fitted by an exponential function. Summarizing the available experimental works in literature, it is still unclear how the shape and size of the densified region depends on microstructural or mechanical properties and, if so, how they control the shape and size of the densified region.

Here, modeling and simulation can be very helpful in studying the effect of selected phenomena on the materials response under a specific loading condition. The indentation of foams was addressed by Needleman et al. based on the Deshpande–Fleck constitutive model [21], by which the effect of plastic compressibility on the nominal hardness H/σ_0 and the hydrostatic pressure was studied. The nominal hardness was found to increase progressively with decreasing plastic compressibility (increasing plastic dilatancy parameter α), which was identified as the main origin, whereas the reduced elastic stiffness E/σ_0 has only a secondary effect. In this work, the compressibility was discussed in terms of its impact on the hydrostatic pressure and the lowered hardness, but the densification of the material as such was not explicitly addressed. Wang et al. investigated the deformation behavior of closed-cell Al foams under conical indentation combining

experiments and Finite Element simulations [22]. They found a concentration of the deformation near the indented surface for cones of different angles, where the densification was related to pore collapse in the intended region and the tearing of cells.

Although a considerable amount of work went into modeling to support the physical understanding of the deformation behavior of nanoporous metals [17], the literature that deals with the simulation of nanoindentation of nanoporous metals is scarce. Mangipudi et al. investigated the material response of np-Au under multiaxial loading, as it is typical for nanoindentation, using representative volume elements (RVE) obtained from FIB/SEM tomography of np-Au samples and from spinodal decomposition [23]. Farkas et al. carried out an MD simulation of the spherical indentation of a sample produced with spinodal decomposition. A detailed evolution of the densified layer under the indenter addressed the mechanism of pore collapse. Liu et al. used a pyramidal flat tip (frustum) indenter and positioned it near the free edge of the sample [24] to provide a better estimate of the uniaxial yield strength. Numerical simulations using the Deshpande–Fleck model confirmed that the indenter geometry provides a clear distinction of the mean pressure at which a material transitions to inelastic behavior. Kwon et al. analyzed nanoindentation experiments with the expanding cavity model (ECM) as well as an improved ECM [25] and discussed their results along with the observed densification in the surface. They concluded that the densification was confined within the residual impression of the Berkovich indenter and, therefore, the deformation of porous metals by indentation testing can be considered similar to compression testing.

Beyond computationally expensive FE-solid models and MD simulations, FE-beam models are an efficient method to study complex structure-properties relationships [26, 27]. With this technique, nanoindentation has been recently studied with focus on the hardness to yield stress ratio in Ref. [28]. However, the densification below the indenter was not addressed. Therefore, in this work, we will investigate the distribution of densification over depth for a large variety of materials, starting out from the micromechanical model [28]. This avoids assumptions about the evolution of the yield locus and the densification behavior under multiaxial loading conditions, commonly needed in continuum modeling. Furthermore, this approach delivers detailed insights in the role of various microstructural and mechanical parameters. In the "Results and discussion" section, effects of the hardening behavior assigned to the solid phase, surface energy and microstructural parameters will be studied. The latter include microstructural and global descriptors, such as ligament shape, solid fraction, randomization of the ligament network and its connectivity density [17]. In the "Conclusions" section, the observed dependencies obtained with an extended model will be compared to results from nanoindentation experiments,

which are specifically designed to validate the findings from the simulation approach.

Results and discussion

Relevance of microstructural and mechanical parameters

For a qualitative study of the relevance of various microstructural and mechanical parameters on the densification behavior, the FE-beam nanoindentation model without embedding is used, described in "FE-beam nanoindentation model" section. The contour plot of the residual displacement after indentation in Fig. 1(a) shows hemispherical isolines that remind of the expansion cavity model (ECM) [29]. The ECM is based on the assumption that the material that is enclosed by the hemisphere of the size of the contact radius. This region is in a state of hydrostatic pressure and deforms incompressible for an elastic-perfectly plastic body. In this case, the radial displacement of particles lying on the boundary of the cavity must accommodate the volume of material displaced by the indenter during an increment of penetration dh . However, as concluded from experimental results by [25], this assumption does not hold for np-Au and this can be confirmed by Fig. 1(a). The deformation localizes within the cavity while the deformation outside is negligible, contradicting the assumption of volume conservation in the ECM. Furthermore, the displacement magnitude that is defined by the ECM at the boundary of the cavity is located far

inside the cavity (red dashed curve), which indicates a compaction of the material near the indenter.

The measurement of the densification profile after [19] requires visualizing the residual deformation after unloading, as shown Fig. 1(b). Qualitatively, a parabolic shape appears as a good approximation for the displacement isolines. However, comparing the parabolic segments with the aspect ratio as introduced by Briot and Balk (white curves) with the deformation contour in the unloaded state (see e.g. blue dashed curve), the segments intersect the isolines of deformation. Averaging within a segment therefore can lead to averaging over a range of relative densities. Apparently, the densification isolines in the simulation are not self-similar. Due to the difference found from the comparison with the shape of Briot and Balk [19], their shape potentially depends on material properties and structural properties of the indented material.

Furthermore, it is of interest how the yield stress $\sigma_{y,s}$, work hardening $E_{T,s}$ and surface energy γ individually control the densification behavior of np-Au in an indentation test. To this end, the model presented in Ref. [28] is extended by including surface energy [15], which also has an effect on the plastic Poisson ratio. The surface energy is modeled by adding a rubbery tube around the cylindrical elements defining the metallic ligaments, which superimpose an axial compressive stress that remains constant during elastic-plastic deformation. The value of the pre-stress is defined by the surface energy and the ligament radius, see Ref. [15] for details. We use a parameter set of $E_s = 80$ GPa, $\nu_s = 0.42$, $\sigma_{y,s} = 200$ MPa, $E_{T,s} = 1$ GPa, $A = 0$,

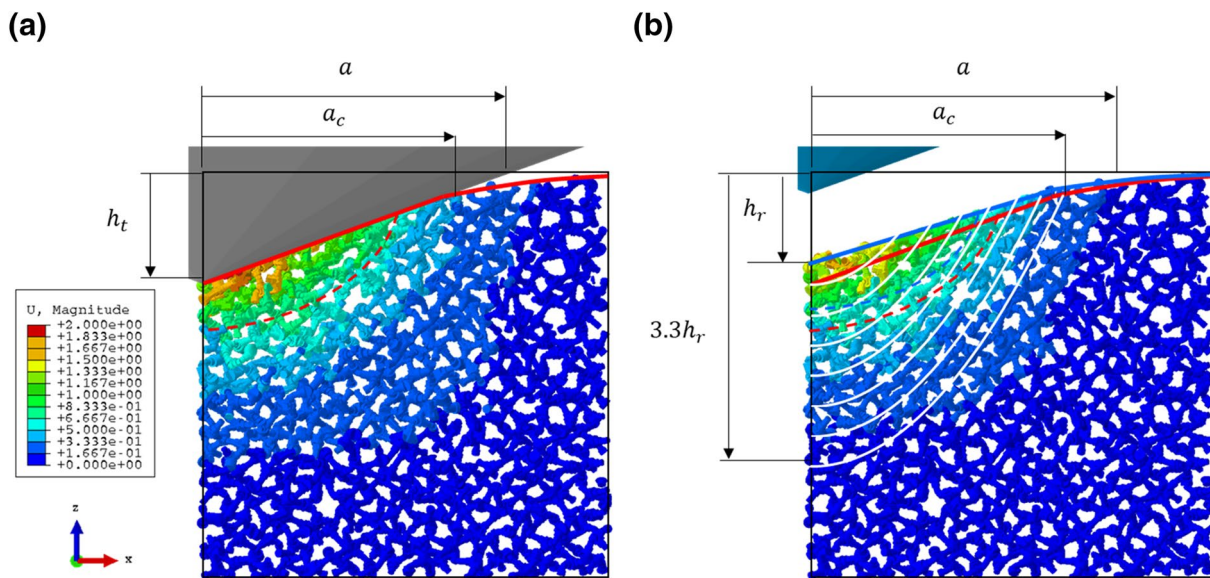


Figure 1: (a) Contour plot of the displacement field under load for $E_s = 80$ GPa, $\nu_s = 0.42$, $\sigma_{y,s} = 200$ MPa, $E_{T,s} = 6$ GPa, $A = 0.23$, and $\zeta = 0$. The red dashed curve corresponds to the displacement that is applied to the boundary of the cavity in the ECM according to Ref. [29] with maximum depth h_t and radius of the cavity a . (b) Residual displacement after removal of the indenter with the effective surface after unloading indicated by the blue curve. The distance from the red to the blue curves correspond to the elastic recovery from maximum depth h_t to the residual depth h_r . White parabolic curves correspond to the shape of the segments for density analysis after Ref. [19].

$\zeta = 0$, and $\gamma = 0\text{J/m}^2$ (off), similar to Ref. [15]. The residual displacement after unloading of the indenter is shown in Fig. 2, labeled as “Reference”. The gradient of the displacement field indicates the degree of densification, i.e. the wider the displacement field spreads into the specimen, the lesser is the local densification.

Relative to the reference model, shown in Fig. 2(b), the variation of one parameter at a time reveals that an increase of the yield stress leads to a drastic concentration of the densification towards the contacted surface, Fig. 2(a). The activation of the surface energy with a value of 1.4J/m^2 (on) counteracts this effect, Fig. 2(c). This is consistent, because the surface energy reduces the yield stress in the ligament and the plastic Poisson ratio in macroscopic compression [15]. The amount of reduction depends on the ligament size and the applied plastic strain. For ligament sizes in the range of 40 to 70 nm, this effect is significant, whereas for larger ligament sizes $\gtrsim 150$ nm, it becomes negligible. Because for the smaller ligament sizes, the effect on the densification behavior is already

small compared to a variation of the yield stress, the surface energy and the discussion of possible size effects arising from this parameter can be omitted in the following. In contrast, an increase of the work hardening rate as shown in Fig. 2(f) acts inverse to the yield stress and has a comparable impact on the densification behavior. Therefore, the focus should be placed on the yield stress and the inverse work hardening rate.

The structural parameters that define the degree of randomization, Fig. 2(d), and cut fraction, Fig. 2(e), seem to have overall little or no effect on the densification of the material. Note that for large cut fractions, the random cutting can create disconnected ligaments or clusters of ligaments that are fully detached from the load bearing ligament network. One of those detached pieces can be seen in Fig. 2(e) above the indented surface. In addition, the effect of friction has been studied relative to the reference with friction coefficients of $\mu = 0, 0.5$ and 1.0 , see Fig. S3. Although this increased the hardness by $\sim 10\%$, the effect in the densification was negligible.

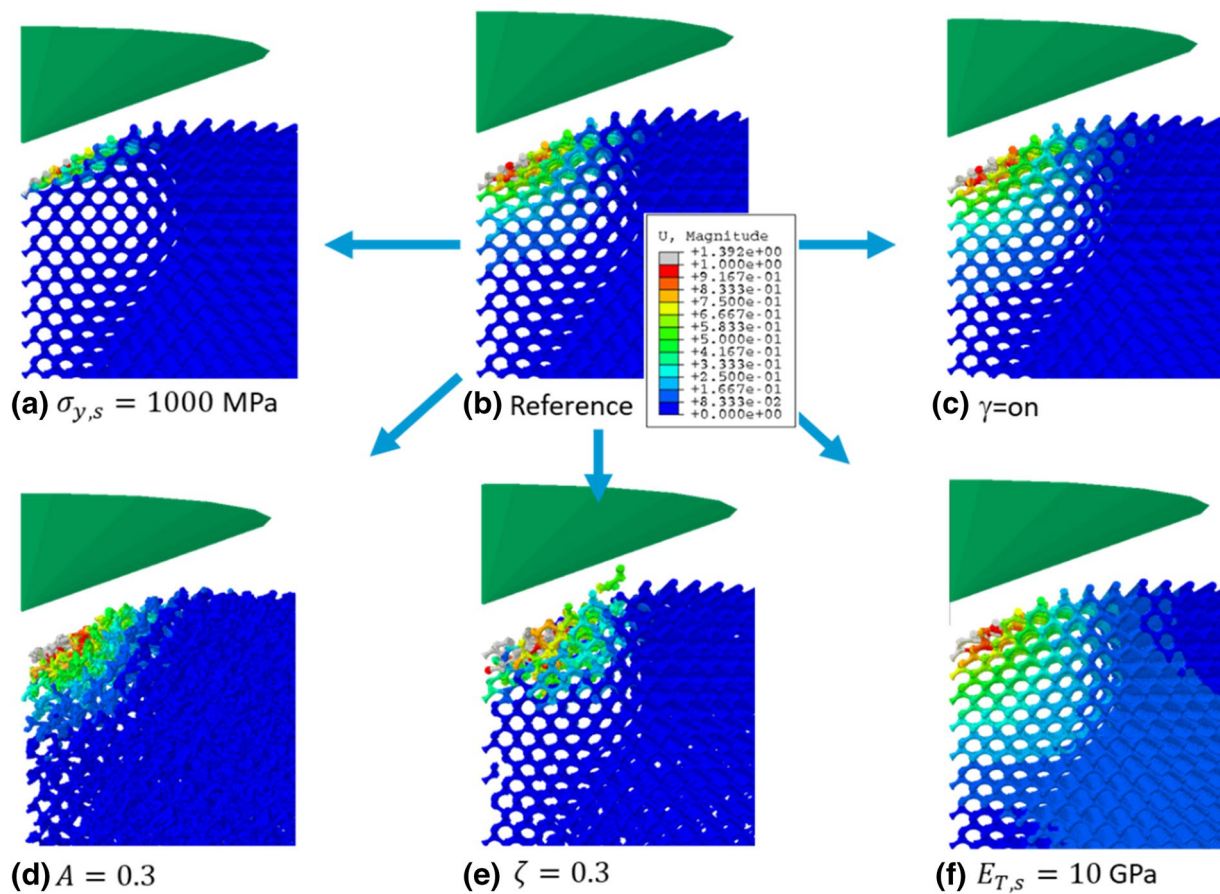


Figure 2: Qualitative study of the effect of different parameters on the residual displacement. The 3D RVE is rotated around the symmetry axis into $\langle 110 \rangle$ direction, allowing to look through the open pores of the diamond structure. The gradient of the displacement field indicates the degree of densification. Relative to the reference case (b), defined by $\sigma_{y,s} = 200$ MPa, $E_{T,s} = 1$ GPa, $A = 0$, $\zeta = 0$, and $\gamma = \text{off}$, changes in the plastic properties (a) and (f) show largest effects, followed by the surface energy (c). The structural parameters defining the randomization $A = 0.3$ in (d) and partial cutting of the ligaments $\zeta = 0.3$ in (e) seem to have little or no effect.

This study provides a first impression of effect of various parameters with respect to the densification of np-Au during nanoindentation. Clearly, the ratio $E_{T,s}/\sigma_{y,s}$ is the most important parameter controlling the densification. This is in line with the findings [28], where this ratio was found to be the primary input for the prediction of the nominal hardness. The scaling law for macroscopic work hardening to yield stress ratio E_T/σ_y was found to depend only on the properties of the solid phase and the initial solid fraction φ_0 in the form

$$\frac{E_T}{\sigma_y} = b\sqrt{\varphi_0} \left(\frac{E_{T,s}}{\sigma_{y,s}} \right)^\beta, \quad (1)$$

with $b = 1.514$ and $\beta = 0.7$ [28]. In this relation, the macroscopic yield stress σ_y and work hardening rate E_T are determined from a linear fit of the stress vs. plastic strain response under macroscopic compression for $0.01 \leq \varepsilon_p \leq 0.2$. Based on Eq. (1) it can be speculated that the resistance of the indented volume is controlled by E_T/σ_y and, according to the qualitative outcome of Fig. 2 it is conceivable that the densification spreads deeper into the material, the stronger the material work hardens. Furthermore, the microstructure seems to be sufficiently represented by the initial solid fraction φ_0 . Therefore, the effect of microstructure and mechanical properties might be sufficiently represented by the ratio E_T/σ_y , which can be determined from macroscopic compression or micropillar testing. Therefore, the set of inputs to be varied can be limited to the initial solid fraction φ_0 and the ratio $E_{T,s}/\sigma_{y,s}$, which considerably reduces the number of simulations from ~ 200 in Ref. [28] to ~ 20 in this work.

Parametric study

Equation (1) suggests to relate the shape of the densified region after nanoindentation to the ratio of $E_{T,s}/\sigma_{y,s}$ and φ_0 or to the macroscopic property ratio E_T/σ_y , which can be measured e.g. by macro compression or micropillar testing. The latter has the advantage of testing a similar sized volume of material as nanoindentation. Both types of tests can be used to validate the modeling results. For a quantitative investigation of the effect of E_T/σ_y on the densification behavior, we carried out simulations for four different ligament shapes G_{21} , G_{23} , G_{33} , G_{43} , see Table 1, and Ref. [30, 31] for more details. These selected shapes are concave ($r_{\text{mid}}/r_{\text{end}} = 0.5$) or cylindrical ($r_{\text{mid}}/r_{\text{end}} = 1.0$) and have different radii r_{end} in the connecting nodes, Table S1 and Fig. S1. They define structures of initial solid fractions ranging from low to high solid fractions ($0.12 \leq \varphi_0 \leq 0.46$). In addition, for each initial solid fraction, the ratio $E_{T,s}/\sigma_{y,s}$ was varied from 5 to 200, which takes into account that for large ligament sizes, the yield stress of np-Au tends to very low values while the work hardening rate remains finite.

The results shown in Fig. 3 confirm that the shape of the densification field depends mainly on the macroscopic property

TABLE 1: Selected ligament geometries as defined in Ref. [30], described by radius at ligament end r_{end} , measured relative to the unit cell size, and mid-to-end ratio $r_{\text{mid}}/r_{\text{end}}$. The value of the initial solid fraction φ_0 applies to the perfect diamond structure before randomization.

Ligament shape	$r_{\text{end}}/a[-]$	$r_{\text{mid}}/r_{\text{end}}[-]$	$\varphi_0[-]$
G_{21}	0.125	0.5	0.1232
G_{23}	0.125	1.0	0.2635
G_{33}	0.15	1.0	0.3574
G_{43}	0.175	1.0	0.4565

ratio E_T/σ_y . The dependence for the penetration depth shown in Fig. 3(a) is nonlinear, changing from a flat to a tipped shape with increasing E_T/σ_y that saturates for large values. As shown in Fig. 3(b), the degree of densification can be represented by an exponential decay function. This implies that the local densification decreases for increasing E_T/σ_y while it is spreading over a larger volume. In other words, the lower E_T/σ_y is, the closer the densified region moves to the surface and the better it can be detected in an experiment.

Nanoindentation and FIB sectioning

For the experimental validation it is of interest to prepare samples with low and high values of E_T/σ_y . At a given solid fraction of $\varphi_0 \approx 0.3$, an increasing ligament size from ~ 20 to ~ 150 nm leads to a decreasing yield stress that can take very low values. At the same time, the work hardening rate also decreases but remains non-zero [5]. By increasing the solid fraction it is possible to increase the yield strength while reducing the work hardening rate to values close to zero [32]. Combining both strategies allows for validating our findings by deliberately placing samples in the lower and in the upper range of E_T/σ_y .

For performing nanoindentation and FIB sectioning followed by image analysis, np-Au samples are produced by electrochemical dealloying. For details we refer to Refs. [32, 33]. Samples #1 and #2 were produced from a Au25Ag75 with two ligaments sizes of $L = 35$ and 120 nm [33]. Sample #3 was produced from a Au35Ag65 master alloy [32]. Samples #1 and #2 allow to compare the results with respect to different ligament sizes, whereas a comparison of samples #2 and #3 allow to compare similar ligament sizes for different initial solid fractions.

Before nanoindentation, all samples were polished. Sample #3 showed a high roughness, which was removed by micromachining of the surface by Xenon Plasma beam (Helios G4 PFIB UXe, Thermo Fisher Scientific). Nanoindentation testing was carried out using a Nanoindenter (Nano XP, KLA Tencor) equipped with a diamond Berkovich tip. Indentations were carried out at a constant strain rate of $0.05/s$ to a displacement of $20 \mu\text{m}$, and then holding the load for 10 s followed by unloading. Load–displacement,

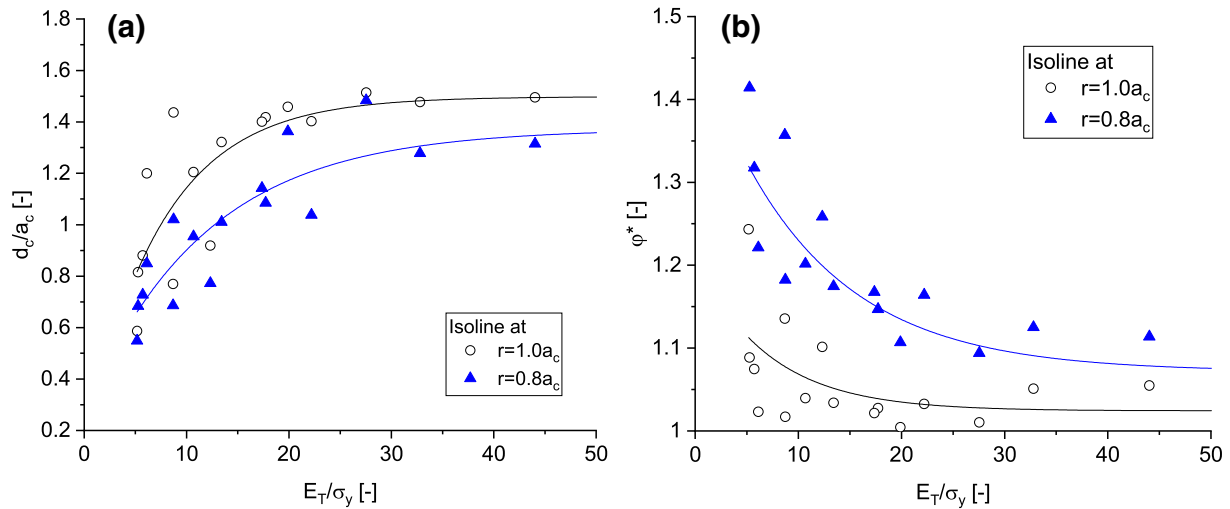


Figure 3: (a) Shape of the densification isolines given as depth to radius ratio d/r , measured at two radial distances from the symmetry axis: $d_c/a_c|1.0$ starts at $r = a_c$ and $d_c/a_c|0.8$ starts at $r = 0.8a_c$ (standard deviations are 0.15 and 0.17, respectively); (b) densification at the selected isolines at $r = a_c$ and $r = 0.8a_c$ as function of E_T/σ_y (standard deviations are 0.05 and 0.11, respectively).

hardness, and modulus curves are shown in Fig. 4(a). Averages for the elastic modulus E and hardness H in Table 2 were obtained from continuous stiffness measurement (CSM) with frequency of 45 Hz and harmonic displacement target of 2 nm. In the load–displacement curves shown in Fig. 4(a), the indents reached 30 to 100 times the average ligament size such that a sufficient number of pores are involved in the densification process under the indent.

For the measurement of the stress–strain behavior, micropillar testing is preferred. In this way it is ensured that the tested volume is comparable to the nanoindentation experiments and both volumes contain similar type and density of features and defects. Micropillar tests from the same samples as used for nanoindentation were available from Ref.[33]. For sample #3 new pillars of 8 μm in diameter are produced, shown in Fig. 4(c), following the same protocol. The measured stress–strain curves are presented in Fig. 4(d) for which the mechanical properties are collected in Table 2. The Young’s modulus measured from the unloading of the micropillars, the yield stress and work hardening rate are denoted by E_u , σ_y , and E_T , respectively. Interestingly, the different ligament size (samples #1 and #2) lead to similar ratios of E_T/σ_y , E/E_u and H/σ_y , whereas these values considerably differ for the two different initial solid fractions (cf. samples #2 and #3). Furthermore, the values of E_T/σ_y as determined from micropillar testing agree very well with the flow curves measured in Ref. [32], from which ratios of 24 and 0.4 are obtained for the samples of $\phi_0 = 0.25$ and 0.35, respectively. Because the E_T/σ_y ratio controls the densification, we can argue that the changes in E/E_u and H/σ_y , which clearly distinguish samples #1 and #2 from sample #3, are directly related to the distribution of densification under the indenter.

Densification analysis

The indentation-induced densification was characterized via inspection of cross-sectional cuts made perpendicular to the indented surface, shown in Fig. 4(b). SEM imaging and FIB milling were performed using a dual-beam system (Nova Nanolab 200, FEI Corp.) equipped with a platinum (Pt) gas injection system. Depositing a Pt layer on the indentation prevented the subsequent exposure of the analyzed surface to the Ga + ion beams, which has been reported to lead to coarsening of the ligament structure [34]. Backscattered electrons using a low voltage (5 kV) were utilized to maximize visibility and to ensure appropriate contrast at the edge of the ligaments. Figure 4(b) shows an SEM micrograph taken at an angle of 52 degrees relative to the cross-section of an indent. The dashed lines indicate the edges between the faces of the indent. The inset shows a sketch of the relative positioning of the Pt deposition and the cross-section relative to the indenter triangular contact. The cross section (CS) was terminated at the mid-section of the indent, as indicated by the visibility of the sharp apex.

SEM images of as-prepared samples #1–3 were analyzed. The magnification was chosen such that the resolution of the ligaments was comparable. The approach consists of several steps for which the details can be found in Ref. [20]. First, shadows and gradients caused by the tilt angle are removed using the Niblack algorithm with a local segmentation area with radius of 15 pixel. The local solid fraction maps were calculated using a scan box size of 50×50 pixel. To calculate the densification map, a reference solid fraction was calculated from a larger rectangular scan box, far away from the indent, surface, and bottom part. The color map of these binarized images represents the distribution of the solid fraction in arbitrary scaling. It was

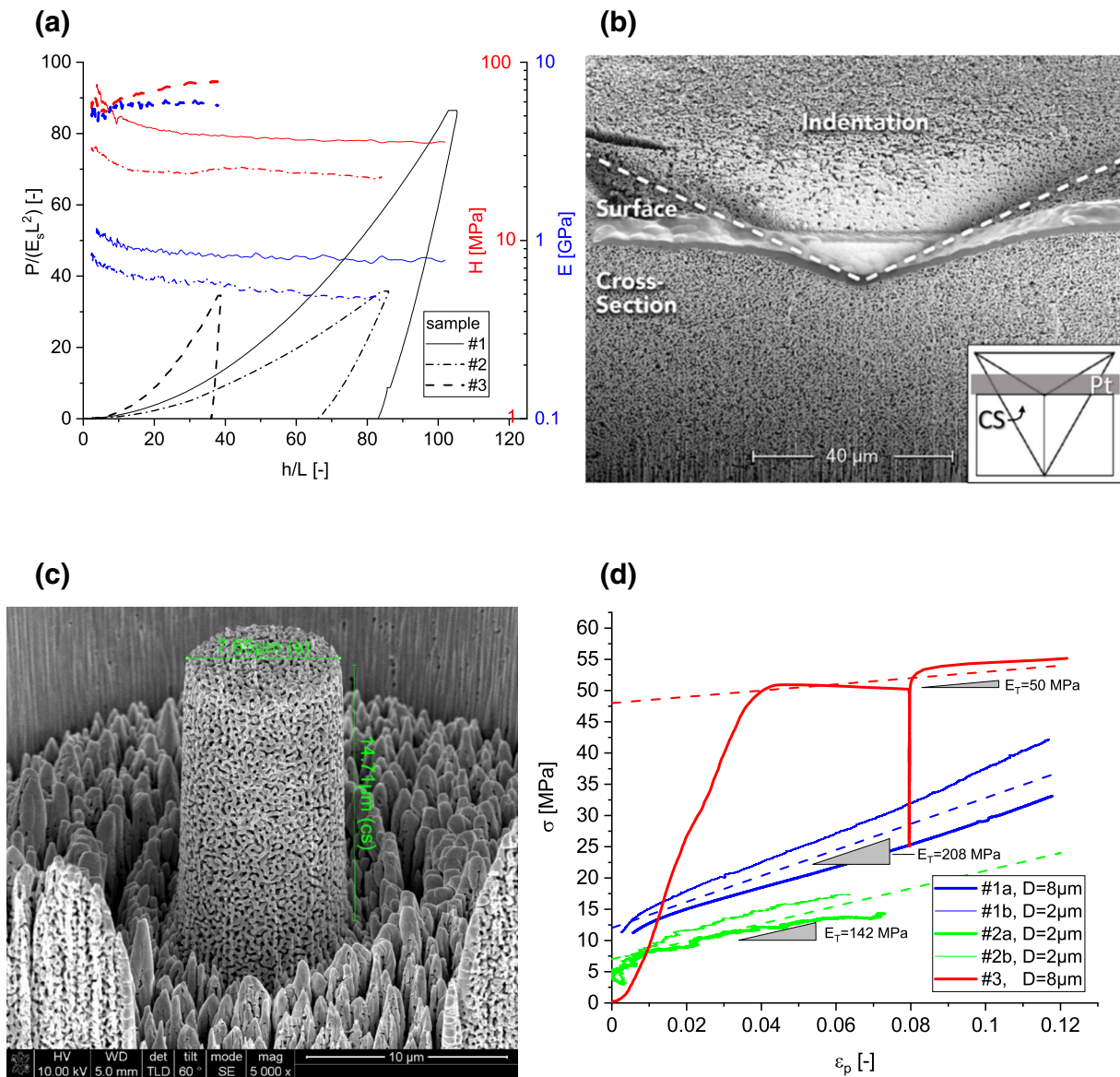


Figure 4: (a) Load–displacement, hardness, and modulus curves from the nanoindentation tests on samples #1–3. Load P and indentation depth h are normalized by Young’s modulus of Au ($E_s = 80$ GPa) and ligament size L . (b) SEM micrograph of a typical cross-section analyzed in this study. Angle of view is 52 degrees relative to the cross-sectional surface. The dashed lines indicate the edges between the faces of the indent. As confirmed by the sharp apex of the indent, the cross section was carried out until the mid-point of the indentation. (c) Micropillar of 8 μm in diameter produced from sample #3, the surface quality after micromachining with the PFIB is visible at the top face of the pillar; (d) stress-plastic strain curves measured from the micropillar tests after subtracting the elastic strains computed with the modulus E_u from unloading.

TABLE 2: Overview of investigated samples and properties as measured by nanoindentation and micropillar testing.

Sample #	φ_0 [-]	L [nm]	H [MPa]	E [MPa]	E_u [MPa]	σ_y [MPa]	E_T [MPa]	E_T/σ_y [-]	E/E_u [-]	H/σ_y [-]
1	0.25	35	38	822	2700	12	208 ± 41	17.3 ± 3.4	0.30	3.2
2	0.25	120	23	527	1250	7	142 ± 33	20.3 ± 4.7	0.42	3.3
3	0.35	106	72	5850	3900	48	50 ± 25	1.04 ± 0.5	1.50	1.5

shown in Ref. [20] that an absolute scaling is not needed, as long as only densification isolines shall be extracted. For a visual representation of the densification in Fig. 5, the values of the

color map are overlaid onto the binarized image. This produces a non-colored boundary, which is half the size of the scanbox. The resulting color map of the densification field in Fig. 5 is

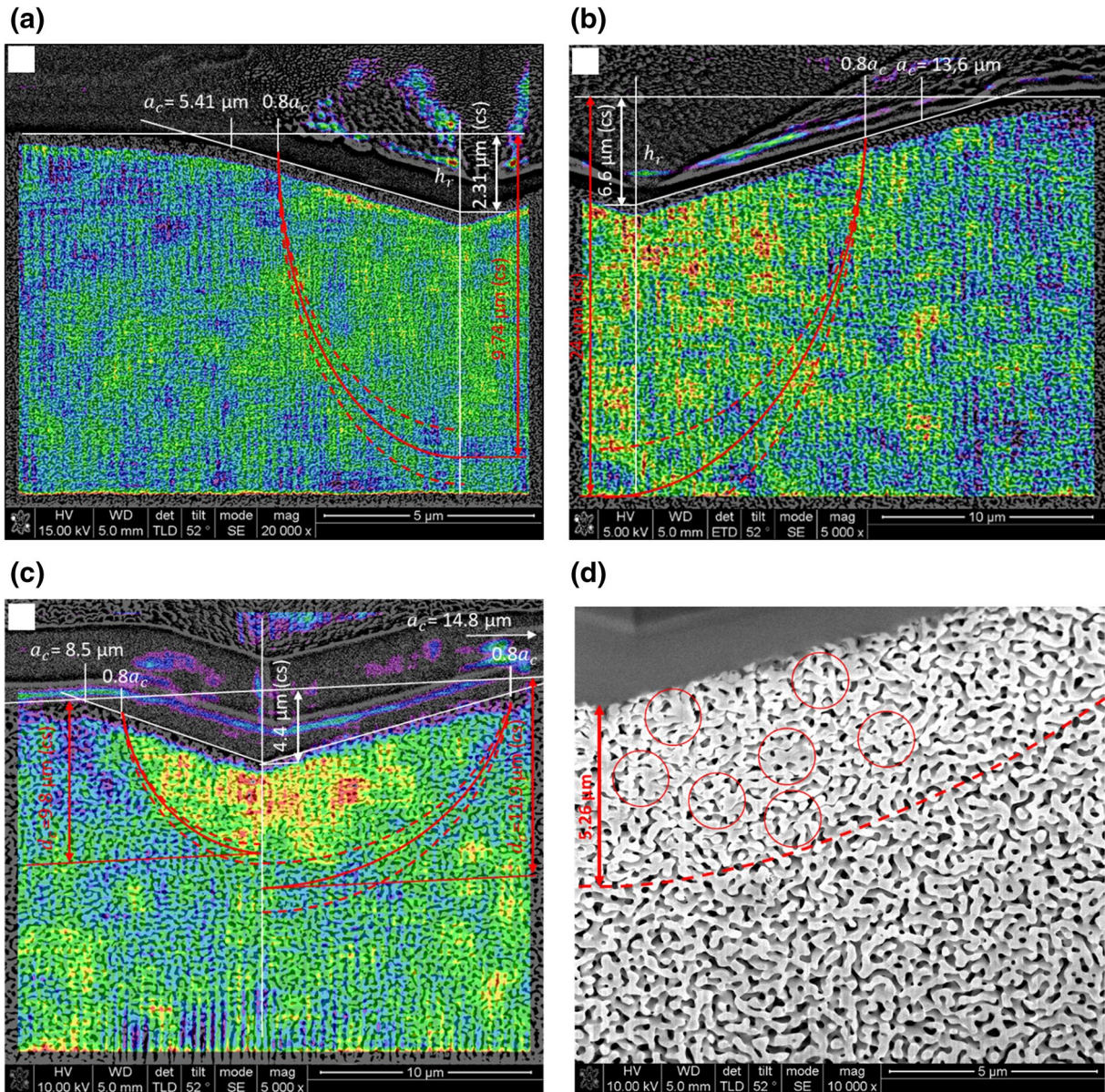


Figure 5: Binarized SEM images with overlaid densification $\varphi^* = \varphi/\varphi_0$ as color map (arbitrary scaling) for (a) sample #1 ($\varphi_0 = 0.25, L = 35$ nm), (b) sample #2 ($\varphi_0 = 0.25, L = 120$ nm) and (c) sample #3 ($\varphi_0 = 0.35, L = 106$ nm). The scan box size was 50×50 pixel, displayed as a white box in the upper left corner. Estimates for the shape of the isolines and error bars are added as red solid and dashed curves, respectively. (d) Zoom-in of the densified region of sample #3 showing multiple contacts below the surface.

still irregular and reflects the inhomogeneity and microstructural randomness of the material. The red solid curves represent isolines drawn as guide to the eye, starting from the surface at $r = 0.8a_c$ towards the symmetry axis. The red dashed curves indicate the uncertainty that results from the inhomogeneity of the color map, from which the error bars in the quantitative analysis are derived.

For samples #1 and #2, the chosen resolution limited the analyzed region to a half of the cross-section. A visual comparison of Fig. 5(a) and (b) confirms that the shape of the

densified region is very similar and appears tipped, even in the tilted perspective. This is in agreement with the similar E_T/σ_y values for sample #1 and #2, which are expected to produce larger aspect ratios $d_c/a_c|_{0.8}$, see Fig. 3(a). In contrast, sample #3, presented in Fig. 5(c), clearly shows a much flatter region of densification that is concentrated closer to the indented surface. Also, the transition into the undeformed material below is more pronounced than for samples #1 and #2. Sample #3 shows a significant asymmetry in the contact radius and in the densification map, which is

treated by separate estimates for the densification isolines. For this sample, multiple contacts can be found in the densified region below the surface, see Fig. 5(d). The depth of this region is comparable to the densified region visible in the color map in Fig. 5(c).

The results for $d_c/a_c|_{0.8}$ as function of E_T/σ_y are shown in Fig. 6 along with the data from the simulations. First of all, the results confirm that the shape of the densified region depends on E_T/σ_y as predicted by the numerical simulations. In contrast to the initial solid fraction φ_0 , the ligament size has no effect for the investigated samples. Compared to the simulations, the experimental data are shifted to higher values. This means that the depth of the densified region penetrates about a factor of 2 deeper as it was predicted by the numerical model. For sample #3, this could be explained by the formation of contacts that limits a further approach of neighboring ligaments during the ongoing deformation. However, in samples #1 and #2, the deformation is distributed deep into the material, such that no formation of contacts is visible and in this case the reason for the underprediction remains unclear.

Independent of the this underprediction, we could confirm that the normalized depth of the densification field $d_c/a_c|_{0.8}$ increases with increasing E_T/σ_y . For the samples investigated in this work, this parameter can be varied via the solid fraction, whereas it is not sensitive to the ligament size. From the stress–strain curves provided in Ref. [32], it can be deduced that the strong variation of E_T/σ_y results from an increase in the yield stress σ_y , while at the same time the work-hardening rate E_T decreases for increasing initial solid fraction. This has a strong effect on the depth and degree of densification below the indenter.

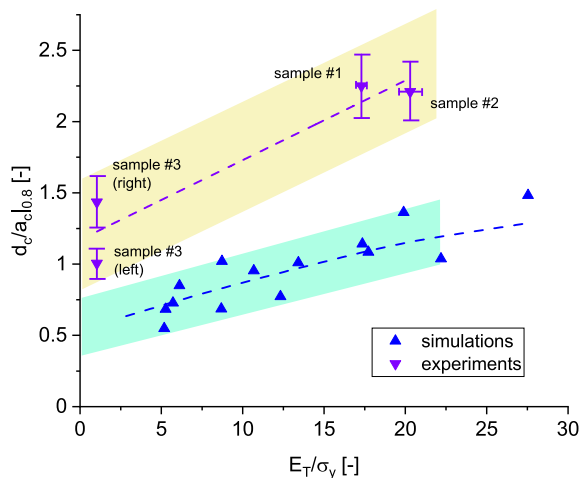


Figure 6: Aspect ratios of the densification isolines at $r = 0.8a_c$ compared with the simulation results.

Conclusions

In this work, we investigated the densification behavior of nanoporous metals in nanoindentation. With the help of a two-scale model and under the assumption of axisymmetric deformation, the displacements of the FE-nodes were projected onto a single cross-section. This allowed for a continuous mapping of the discrete displacement data and the computation of a smoothly distributed deformation gradient and densification field in cylindrical coordinates. Following the literature [18–20], in the experimental part of this work the densification under the indenter was made assessable to SEM by FIB milling. We tested a large range of ligament sizes from 35 to 150 nm and initial solid fractions of 0.25 to 0.35. Following the procedure described in Ref. [20], color maps for the densification were computed that allowed to determine the shape of the densification isolines by visual inspection. The work hardening rate to yield stress ratio E_T/σ_y was measured via micropillar compression testing.

The simulations showed that the penetration depth of the densification field into the volume is mainly controlled by the ratio of the macroscopic work hardening rate to yield stress E_T/σ_y . This parameter includes the work hardening behavior of the solid phase and the solid fraction. For the characterization of the shape of the densification field, the aspect ratio of the densification isolines originating at the contact radius a_c and at $0.8 a_c$ are used. The shape of the outer isoline allows for a comparison with the approach of the data with those from Briot and Balk [19]. It is found that isolines further inside are not self-similar and they tend to align with the indented surface moving inwards. At the same time, the densification continuously increases, i.e. a maximum below the surface as reported by Ref. [19] could not be confirmed. Similarly to the aspect ratio of the isoline d_c/a_c , the densification value on the isolines is a function of E_T/σ_y , which can be modeled with an exponential decay function. For low E_T/σ_y , internal contacts become relevant and this limits the degree of compaction.

With regard to the dependence of the E_T/σ_y ratio, the experimental data confirm the trend of an increase of $d_c/a_c|_{0.8}$ with increasing E_T/σ_y , as derived from the numerical simulations. In our experiments, the initial solid fraction φ_0 delivered a substantial variation of E_T/σ_y , whereas the ligament size had no influence. The enhancement of local densification and internal contacts during compression for increasing φ_0 and decreasing E_T/σ_y is also in agreement with the findings of Liu et al. [35], who reported an unexpected transition from homogeneous to localized deformation under compression as φ_0 increases to above $\sim 1/3$. As can be seen from Eq. (1), it should also be possible to modify E_T/σ_y via $E_{T,s}/\sigma_{y,s}$, i.e. the work hardening behavior of the solid phase at constant φ_0 . This is supported by the results from Leitner et al. [18], where the distribution of the densification field was considerably changed from localized to

extended alone by the temperature at which the nanoindentation was performed.

The simulations underpredict the experimental results for $d_c/a_c|_{0.8}$. This could in part be explained by contacts in the densified material that form at low values of E_T/σ_y . Independent of this, the FE-beam modeling approach might have some limitations, although the nodal correction [31] was used. A solid model with internal contacts could be able to close this gap, but such a model is computationally demanding. As simplification, the knowledge from this work allows to further reduce the number of required simulations considerably, because it should be sufficient to vary just one out of the three parameters solid fraction ϕ , yield stress $\sigma_{y,s}$, or work hardening rate $E_{T,s}$. Still, such simulations imply the availability of highly efficient and scalable FE codes that allow to model realistic microstructures including internal contacts.

On the experimental side, further work on the image processing as pointed out in Ref. [20] would be very beneficial for the reliable extraction of densification profiles. Images of a FIB cross-section taken at an inclination of 52° lead to different illumination and gradients when samples with very different ligament sizes are analyzed. In part, this could be resolved with the Niblack algorithm, but the quality of segmentation is still not sufficient for a robust extraction of the densification profiles via line scans. Here, the application of deep neural networks as e.g. developed in Ref. [36] could be very useful.

Methods

The modeling of nanoindentation of np-Au is carried out in two ways. For qualitative investigations, the quarter model based on the RVE as presented in Ref. [28] is used to study the effect of various parameters on the densification under the indent. Second, a more sophisticated model for a refined quantitative analysis of the densification is presented. Here, the micromechanical model is embedded in a continuum model that delivers the elastic foundation of a cylindrical volume. Finally, the densification analysis is described for providing measures that can be used for comparison with experimental results.

FE-beam nanoindentation model

The FE-beam model for nanoindentation without embedding is shown in Fig. S2 and is described in detail in Ref. [28]. Throughout this work, a rigid indenter with a cone angle of 140.6° is used. The modeling of the nanoporous material and builds on ordered and randomized diamond structures that were originally established as ball-and-stick models [26, 37] and generalized to ligament shapes that can have convex, cylindrical, or concave shape [30, 31]. This approach allows predicting the macroscopic elastic–plastic deformation behavior of np-Au for

given properties, denoted in the following with subscript s for the solid, namely Young's modulus E_s , Poisson's ratio ν_s , yield stress $\sigma_{y,s}$, and work hardening rate $E_{T,s}$. The degree of the randomization of the structure is defined by the parameter A , which applies a random distortion of the connecting nodes as fraction of the unit cell size [26]. Random cutting of ligaments is possible by choosing a cut fraction ζ , by which a percentage of the ligaments are randomly selected and disconnected by element removal. In this way, the average coordination number per node and the scaled genus density of the ligament network can be continuously tuned from fully connected (diamond structure) down to the percolation to cluster transition [27].

Spherical-parabolic ligament shapes are represented by the mid-to-end ratio of the ligament radius $r_{sym}^* = r_{mid}/r_{end}$ [30], see Table S1 and Fig. S1. With the incorporation of the nodal correction by [31], the FE-beam model allows for predicting elastic–plastic stress–strain curves that are in good agreement with a FE-solid model at the efficiency of the FE-beam model. The nodal correction is applied to those FE beam elements, which form the nodal region connecting several elements, colored in orange in Fig. S1. The extension of this zone and the element properties are defined such that the mechanical behavior of foams with stout struts, as depicted in Fig. 1, can be correctly predicted. For details on the nodal correction, the reader is referred to Ref. [31].

The Poisson's ratio under macroscopic compression depends on the randomization as well as the connectivity of the structure [26, 27]. It is expected that the parameters defining the randomization A and cut fraction ζ both can have an effect on the densification of the material during indentation. For simplicity, the model was generated such that the unit cell size corresponds to a unit size of 1 mm [28]. Realistic microstructural dimensions of the ligament and the pore size can be achieved by self-similar scaling of the model to a desired characteristic size, e.g., a ligament diameter of 20–150 nm [5]. With the exception of the surface energy, the elastic–plastic material law does not account for size effects, the resulting macroscopic behavior is not affected by such a scaling. Where relevant, the surface energy is introduced indirectly by an axial compressive residual stress in the ligaments, which is computed for the chosen nominal ligament size [15].

The nanoindentation simulation includes multiple contacts of individual ligaments with the indenter, which leads to convergence problems in the early stages of an implicit FE simulation approach. This problem is solved by using an explicit integration scheme in a dynamic simulation [28], which efficiently copes with the individual contacts as they emerge. The maximum indentation depth h_t is set to a depth of 2 diamond unit cells, which corresponds to 25% of the model dimension. Fig. S2 shows an example of an indentation simulation into a RVE, built as a quarter model with symmetry boundary conditions. It

consists of $8 \times 8 \times 8$ diamond unit cells with a randomization of $A = 0.23$ and a cut fraction of $\zeta = 0$, i.e. the ligaments are randomly distorted but remain fully connected. It can be seen that the displacement within the ligament network is concentrated within the boundaries. Due to sink-in, a small negative radial displacement appears at the free boundary near the surface of the model, as the material is drawn inwards towards the indent. This radial displacement at the boundary is around 5% of a unit cell size.

Two-scale nanoindentation model

For the model presented in the "FE-beam nanoindentation model" section, the translation of the displacement field into the depth can become unsteady around the symmetry axis, when the structure is randomized. This is an effect of the limited number of unit cells along the depth coordinate, which leads to an inhomogeneous densification in case of distorted or broken load paths, see also Fig. 1. This is amplified around the symmetry axis, because a larger pore is mirrored four times by the symmetry boundary conditions. For a refined analysis, a new nanoindentation model is developed that delivers a more continuous deformation field. To this end, the micromechanical model presented in the "FE-beam nanoindentation model" section is extended in the xy-plane towards $16 \times 16 \times 8$ unit cells and then cut to a cylinder with a radius of 8 unit cells, labeled as FE-beam model in Fig. 7. In analogy to the window-method [38], the FE-beam model (152,482 beam elements, type B31) is embedded in a FE-solid model (14,123 tetrahedral elements, type C3D10) that is generated in Abaqus CAE with an overlap of 0.25 unit cells using the *EMBED command in Abaqus. For the elements of the embedded FE-beam model, isotropic elastic-plastic deformation behavior with elastic properties E_s, ν_s , yield stress $\sigma_{y,s}$ and linear work hardening with work-hardening rate $E_{T,s}$ is assumed, where the index s denotes the mechanical properties of the solid phase.

Boundary conditions are applied to the bottom nodes of the FE-solid model, fixing the displacements in all degrees of freedom. The elastic properties of the solid elements are set to the effective macroscopic elastic properties of the micromechanical model computed from macroscopic compression of 0.1% strain a cubic RVE ($8 \times 8 \times 8$ unit cells) assuming isotropic elastic behavior. Figure 7 shows the contour plot of the residual deformation after indentation, which is concentrated within the FE-beam model. One simulation run requires 230 CPUh and can be solved parallel on 16 CPUs in less than one day.

The cylindrical model, which is loaded by a rigid conical indenter, allows for a circumferential projection and averaging of the nodal displacements of the micromechanical model onto a single cross-section within a cylindrical coordinate system, where R, Z and r, z denote the coordinates of the undeformed

reference configuration and the deformed configuration, respectively. This delivers a smooth and continuous displacement field for vertical displacements $u_z(R, Z)$ and radial displacements $u_r(R, Z)$ shown in Fig. 7(b) and (c), respectively. The projection also averages the remaining anisotropic behavior of the diamond structure after randomization. The comparison confirms that the radial displacements are more than a magnitude lower than the vertical displacements and it is possible to neglect radial displacements in the analysis of the densification. The error $u_{err} = \sqrt{u_z^2 + u_r^2} - |u_z|$ from neglecting the radial displacements is shown in Fig. 7(d). The largest error is $\sim 1\%$ of the maximum displacement, concentrated at the contact radius. Another region of increased error appears inside the volume and is related to the preferred transmission of deformation in $\langle 111 \rangle$ direction, due to the orientation of the ligaments in the diamond structure.

Densification field

Next, we develop an approach that allows for interpolating the displacement field from the discrete positions of the numerical simulation for delivering a continuous mapping of the volume change. This provides access to the densification profile as function of depth and the development of characteristic measures for the in-depth investigation following in the "Conclusions" section. In continuum mechanics, the densification φ^* , which is volume change from an undeformed volume element dV_0 to a deformed volume element dV_1 , can be computed from the deformation gradient $\mathbf{F} = \mathbf{I} + \nabla \mathbf{u}$ as

$$\varphi^* = \frac{\varphi_1}{\varphi_0} = \frac{dV_1}{dV_0} = \frac{1}{\det \mathbf{F}}, \quad (2)$$

where \mathbf{I} is the unit tensor, $\nabla \mathbf{u}$ is the velocity gradient tensor, and \det denotes the determinant of a tensor of second order [39]. It should be noted that after unloading of the indenter, the computed deformation gradient still includes elastic and plastic components, because the inhomogeneous deformation of the indentation process has a residual stress field. For axisymmetry in a cylindrical coordinate system and negligible radial displacements, the deformation gradient simplifies to (Appendix A)

$$\det \mathbf{F} = \left(1 + \frac{\partial u_z}{\partial Z} \right) \quad (3)$$

A polynomial fit of the displacement data $u_z(Z)$ at constant radial coordinate R allows to compute the deformation gradient and the densification by combining Eqs. (3) and (2). Figure 8 presents two examples for the computed densification field for a low and a high value of $E_{T,s}/\sigma_{y,s}$, demonstrating the impact of this parameter on the penetration depth of the densification.

For the analysis of images from experiments, it is useful to have a well-defined reference value for which we can

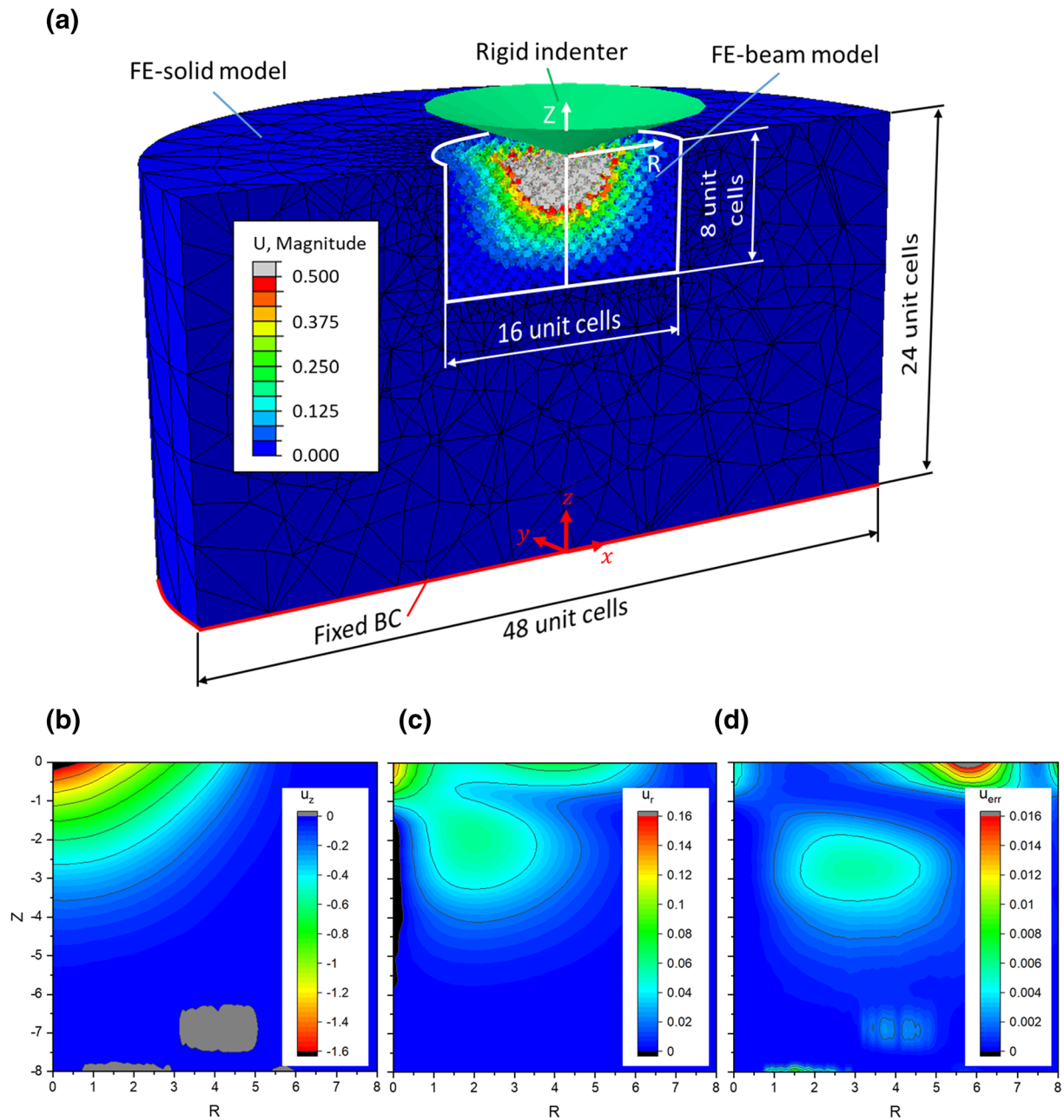


Figure 7: (a) Cut view of the two-scale nanoindentation model with the micromechanical FE-beam model embedded in a FE-solid model. Boundary conditions are applied at the bottom of the FE-solid model far from the micromechanical model. Shown is the magnitude of the residual displacement after unloading of the indenter, (b–d) Mapping of the displacement field onto a cross-section of a cylindrical coordinate system in undeformed configuration (R, Z) with the origin in the top center of the full model with (b) z -displacement, (c) radial displacement, and (d) error for neglecting the radial displacements—note that the color map is scaled by factor 10.

use the position of the contact radius a_c and the densification measured in this point. As seen in Fig. 8, the shape of the isoline can be characterized by the ratio of the two distances d_c/a_c , which increases for increasing $E_{T,s}/\sigma_{y,s}$. However, the densification that is measured at a_c has the highest uncertainty due to neglecting the radial displacements, see Fig. 7(d). Furthermore, the value is naturally close to 1, which makes it

very difficult to reliably detect the distance d_c in the vertical direction. Therefore, we suggest to use the isoline measured at 80% of the contact radius $a_{c0.8}$, which is located in a region with a higher densification gradient. Along this isoline, the data are more robust to scatter, while there is still a detectable sensitivity of the position of this isoline to $E_{T,s}/\sigma_{y,s}$ along the symmetry axis.

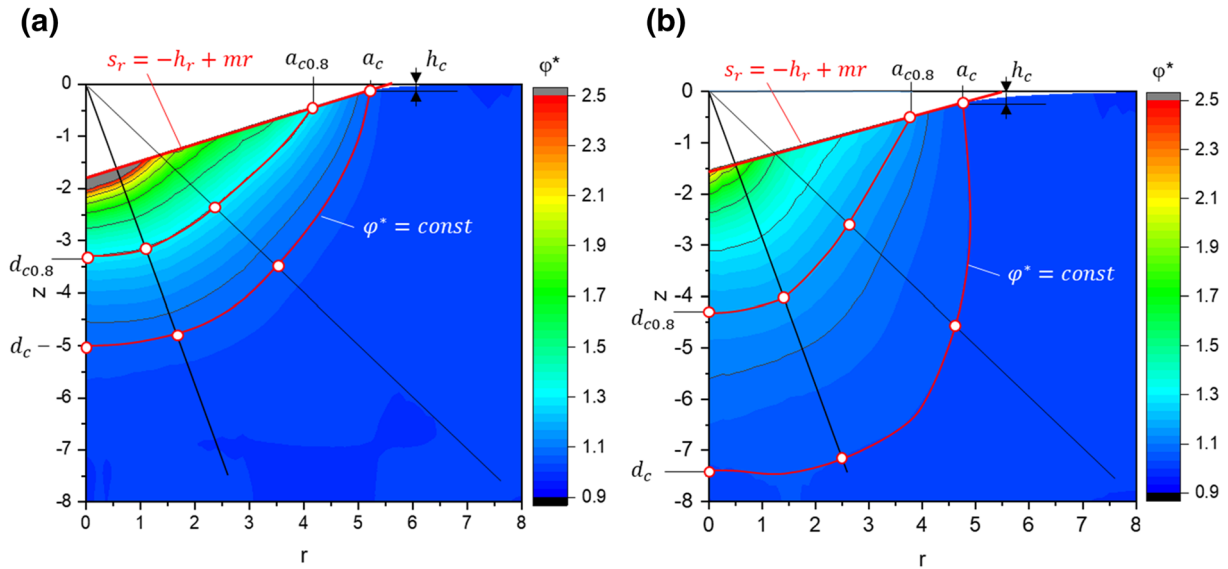


Figure 8: (a) Contour plot of φ^* in the deformed configuration for $\varphi_0 = 0.357$, $\sigma_{y,s} = 200$ MPa, $A = 0.23$. Isolines added in red color allow deriving a measure for the penetration depth of the residual densification field relative to the contact radius. (a) $E_{T,s}/\sigma_{y,s} = 5$, b) $E_{T,s}/\sigma_{y,s} = 50$.

Acknowledgments

The authors acknowledge fruitful discussions with J. Weissmüller, which helped to strengthen the manuscript. M. Ziehmer is gratefully acknowledged for his support of sample preparation with the PFIB.

Funding

Open Access funding enabled and organized by Projekt DEAL. This work was supported by the Deutsche Forschungsgemeinschaft (DFG, German Research Foundation) – Project Number 192346071 – SFB 986 “Tailor-Made Multi-Scale Materials Systems: M³,” project B4, B8, and B2.

Declarations

Conflict of interest The authors declare that they have no known competing financial interests or personal relationships that could have appeared to influence the work reported in this paper.

Open Access

This article is licensed under a Creative Commons Attribution 4.0 International License, which permits use, sharing, adaptation, distribution and reproduction in any medium or format, as long as you give appropriate credit to the original author(s) and the source, provide a link to the Creative Commons licence, and indicate if changes were made. The images or other third party material in this article are included in the article’s Creative Commons licence, unless indicated otherwise in a credit line to the material. If material is not included in the article’s Creative Commons licence and your intended use is not permitted

by statutory regulation or exceeds the permitted use, you will need to obtain permission directly from the copyright holder. To view a copy of this licence, visit <http://creativecommons.org/licenses/by/4.0/>.

Appendix

A. Deformation gradient

In a cylindrical coordinate system the components of $\nabla \mathbf{u}$ can be expressed as [39], p. 62,

$$\mathbf{F} = \begin{pmatrix} 1 + \frac{\partial u_r}{\partial R} & \frac{1}{R} \left(\frac{\partial u_r}{\partial \theta} - u_\theta \right) & \frac{\partial u_r}{\partial Z} \\ \frac{\partial u_\theta}{\partial R} & 1 + \frac{1}{R} \left(\frac{\partial u_\theta}{\partial \theta} + u_r \right) & \frac{\partial u_\theta}{\partial Z} \\ \frac{\partial u_z}{\partial R} & \frac{1}{R} \frac{\partial u_z}{\partial \theta} & 1 + \frac{\partial u_z}{\partial Z} \end{pmatrix}, \quad (\text{A.1})$$

where coordinates (R, Z) and (r, z) denote the coordinates in the undeformed reference configuration and in the deformed configuration, respectively. The variables u_r , u_θ , and u_z denote the displacements in radial, circumferential, and vertical direction. For axisymmetry, $u_\theta = 0$ and $\frac{\partial(\cdot)}{\partial \theta} = 0$, such that Eq. (A.1) can be simplified to

$$\mathbf{F} = \begin{pmatrix} 1 + \frac{\partial u_r}{\partial R} & 0 & \frac{\partial u_r}{\partial Z} \\ 0 & 1 + \frac{u_r}{R} & 0 \\ \frac{\partial u_z}{\partial R} & 0 & 1 + \frac{\partial u_z}{\partial Z} \end{pmatrix}. \quad (\text{A.2})$$

From Eq. (A.2), we obtain

$$\det \mathbf{F} = \left(1 + \frac{\partial u_r}{\partial R} \right) \left(1 + \frac{u_r}{R} \right) \left(1 + \frac{\partial u_z}{\partial Z} \right) - \frac{\partial u_r}{\partial Z} \left(1 + \frac{u_r}{R} \right) \frac{\partial u_z}{\partial R}, \quad (\text{A.3})$$

which serves for the computation of the volume change according to Eq. (3). When the radial displacement u_r and its derivative $\frac{\partial u_r}{\partial R}$ in Eq. (A.3) can be neglected, this equation simplifies to

$$\det \mathbf{F} = \left(1 + \frac{\partial u_z}{\partial Z} \right). \quad (\text{A.4})$$

Supplementary Information

The online version contains supplementary material available at <https://doi.org/10.1557/s43578-022-00870-1>.

References

- J. Weissmüller, K. Sieradzki, MRS Bull. **43**, 14 (2018)
- E.T. Lilleodden, P.W. Voorhees, MRS Bull. **43**, 20 (2018)
- H.-J. Jin, J. Weissmüller, D. Farkas, MRS Bull. **43**, 35 (2018)
- J. Biener, A.M. Hodge, A.V. Hamza, L.M. Hsiung, J.H. Satcher, J. Appl. Phys. **97**, 24301 (2005)
- N. Mameka, K. Wang, J. Markmann, E.T. Lilleodden, J. Weissmüller, Mater. Res. Lett. **4**, 27 (2016)
- K. Hu, M. Ziehmer, K. Wang, E.T. Lilleodden, Phil. Mag. **96**, 3322 (2016)
- L.-Z. Liu, X.-L. Ye, H.-J. Jin, Acta Mater. **118**, 77 (2016)
- J. Biener, A.M. Hodge, J.R. Hayes, C.A. Volkert, L.A. Zepeda-Ruiz, A.V. Hamza, F.F. Abraham, Nano Lett. **6**, 2379 (2006)
- A.M. Hodge, J. Biener, J.R. Hayes, P.M. Bythrow, C.A. Volkert, A.V. Hamza, Acta Mater. **55**, 1343 (2007)
- C.A. Volkert, E.T. Lilleodden, D. Kramer, J. Weissmüller, Appl. Phys. Lett. **89**, 61920 (2006)
- H.-J. Jin, L. Kurmanaeva, J. Schmauch, H. Rösner, Y. Ivanisenko, J. Weissmüller, Acta Mater. **57**, 2665 (2009)
- H.-J. Jin, J. Weissmüller, Adv. Eng. Mater. **12**, 714 (2010)
- H.-J. Jin, J. Weissmüller, Science (New York, NY) **332**, 1179 (2011).
- L. Lühns, C. Soyarslan, J. Markmann, S. Bargmann, J. Weissmüller, Scripta Mater. **110**, 65 (2016)
- L. Lühns, B. Zandersons, N. Huber, J. Weissmüller, Nano Lett. **17**, 6258 (2017)
- L. J. Gibson, M. F. Ashby, *Cellular Solids. Structure & Properties*, 1. ed. (Pergamon Press, Oxford, 1988).
- C. Richert, N. Huber, Materials (Basel, Switzerland) **13** (2020).
- A. Leitner, V. Maier-Kiener, J. Jeong, M.D. Abad, P. Hosemann, S.H. Oh, D. Kiener, Acta Mater. **121**, 104 (2016)
- N. J. Briot, T. J. Balk, MRS Commun. **8**, 132 (2018).
- C. Richert, Y. Wu, M. Hablitzel, E.T. Lilleodden, N. Huber, MRS Adv. **6**, 519 (2021)
- A. Needleman, V. Tvergaard, E. van der Giessen, Acta Mech. Sin. **31**, 473 (2015)
- X. Wang, X. Wang, K. Jian, L. Xu, A. Ju, Z. Guan, L. Ma, ACS Omega **6**, 28150 (2021)
- K.R. Mangipudi, E. Epler, C.A. Volkert, Scripta Mater. **146**, 150 (2018)
- R. Liu, S. Pathak, W.M. Mook, J.K. Baldwin, N. Mara, A. Antoniou, Int. J. Plast. **98**, 139 (2017)
- O. M. Kwon, J. Kim, J. Lee, J.-h. Kim, H.-J. Ahn, J.-Y. Kim, Y.-C. Kim, D. Kwon, Met. Mater. Int. (2020).
- N. Huber, R.N. Viswanath, N. Mameka, J. Markmann, J. Weißmüller, Acta Mater. **67**, 252 (2014)
- N. Huber, Front. Mater. **5**, 5801 (2018)
- N. Huber, Materials (Basel, Switzerland) **14**, 1822 (2021).
- K.L. Johnson, J. Mech. Phys. Solids **18**, 115 (1970)
- C. Richert, A. Odermatt, N. Huber, Front. Mater. **6**, 352 (2019)
- A. Odermatt, C. Richert, N. Huber, A. Odermatt, C. Richert, N. Huber, Mater. Sci. Eng. A **791**, 139700 (2020)
- B. Zandersons, L. Lühns, Y. Li, J. Weissmüller, Acta Mater. **215**, 116979 (2021)
- Y. Wu, J. Markmann, E.T. Lilleodden, Appl. Phys. Lett. **115**, 251602 (2019)
- Y. Sun, T.J. Balk, Scripta Mater. **58**, 727 (2008)
- L.-Z. Liu, Y.-Y. Zhang, H. Xie, H.-J. Jin, Phys. Rev. Lett. **127**, 95501 (2021)
- T. Sardhara, R.C. Aydin, Y. Li, N. Piché, R. Gauvin, C.J. Cyron, M. Ritter, Front. Mater. **9**, 2843 (2022)
- B. Roschning, N. Huber, J. Mech. Phys. Solids **92**, 55 (2016)
- S. Gnegel, J. Li, N. Mameka, N. Huber, A. Düster, Materials (Basel, Switzerland) **12** (2019).
- W.M. Lai, D. Rubin, E. Krempf, *Introduction to Continuum Mechanics*, 3rd edn. (Pergamon Press, Oxford, 1993)

Publisher's Note Springer Nature remains neutral with regard to jurisdictional claims in published maps and institutional affiliations.